Journal of
Materials Chemistry B

PAPER

View Article Online
View Journal | View Issue

Cite this: J. Mater. Chem. B, 2018, 6, 7684

Graphitic porous carbon: efficient synthesis by a combustion method and application as a highly selective biosensor

Bisang Chen,[a] Dejian Chen,[a] Feiming Li,*[ab] Xiaofeng Lin*[c] and Qitong Huang *[de]

Received 14th August 2018,
Accepted 19th October 2018

DOI: 10.1039/c8tb02139b

rsc.li/materials-b

Graphitic porous carbon (GPC) was simply synthesized by a combustion method, in which dry ice was used as the carbon source and magnesium powder was used as the reductant. The whole combustion procedure only took about 10 min without any sophisticated equipment or toxic and corrosive reagents, demonstrating high energy, material, and labour efficiency. The GPC was characterized by powder X-ray diffraction, transmission electron microscopy, nitrogen sorption analysis, and Raman spectroscopy, and the results showed that the obtained GPC had a high degree of graphitization and a high surface area (the surface area and total pore volume of the GPC were 414.87 m^2 g^{-1} and 1.03 cm^3 g^{-1}, respectively). Benefitting from high graphitization, the prepared GPC demonstrated high conductivity for simultaneous determination of dopamine and uric acid with the detection limits of 8.0 nM and 30.0 nM, respectively. Owing to the high efficiency of this method, it may potentially be applied on the scale of industrial production.

1 Introduction

Graphitic porous carbon (GPC) with a highly crystalline structure exhibits fascinating properties, including high surface area and good thermal and mechanical stabilities. In particular, GPC has better oxidation resistance and higher electronic conductivity compared with amorphous carbon, which has made it ubiquitous and indispensable for applications in electrode materials for batteries,[1,2] supercapacitors,[3–5] sorbents,[6,7] and supports for various important catalysts.[8–10] These outstanding characteristics as well as promising applications have boosted interest in searching for new methods for the synthesis of GPC.

Currently, the nanocasting method is one of most powerful methods for GPC fabrication. Nanocasting synthesis consists of two main steps: carbonization and removal of templates and catalysts. First, various hydrocarbons are selected as precursors, and nanoparticles[11,12] or mesoporous silica[13–15] as a hard template, and then graphitized at high temperature (and sometimes under high pressure) or low temperature using metal salts as catalysts; second, the templates or the catalysts are removed after graphitization. For example, Yoon and co-workers[13] synthesized GPC by filling mesoporous silica mesochannels with pitch, and then graphitizing at 2500 °C under flowing argon. However, the approach was energy consumptive. Moreover, the large pore volume and surface area of the GPC were reduced after treatment at high temperatures; in addition, the removal of the silica templates with a corrosive HF process made this method complicated for real applications. Apart from the high temperature graphitization method, catalytic graphitization at lower temperatures with transition-metal ions (*e.g.* Co^{2+}, Fe^{3+}) is an effective approach for *in situ* production of graphitic nanostructures. Gao and co-workers[14] successfully synthesized partially graphitic ordered mesoporous carbon using ferric oxide as the catalyst *via* a triblock-copolymer-templating method. Liu and co-workers[15] prepared highly GPC with the catalyst of Ni; the GPC products showed high conductivity and surface area, and they were applied as the electrode material of electrochemical capacitors with much higher high-rate capacitive performance when compared with activated carbon. However, the complicated fabrication of metal catalysts of these methods still hinders their development. Undoubtedly, it is still highly important to search for complementary synthetic strategies for GPC with extreme performance values.

In this work, we have developed a facile method for preparation of GPC, which could be potentially scaled up, using direct

[a] College of Chemistry and Environmental, Minnan Normal University, Zhangzhou, Fujian, 363000, P. R. China
[b] The MOE Key Laboratory of Spectrochemical Analysis and Instrumentation, College of Chemistry and Chemical Engineering, Xiamen University, Xiamen, 361005, P. R. China. E-mail: Lifeiming0228@foxmail.com
[c] Department of Chemistry, Shantou University, Shantou, Guangdong, 515063, P. R. China. E-mail: Lxf0596@163.com
[d] College of Pharmacy, Gannan Medical University, Ganzhou, 341000, P. R. China. E-mail: hqtblue@163.com
[e] College of Biological Science and Biotechnology, Minnan Normal University, Zhangzhou, Fujian, 363000, P. R. China

combustion of magnesium powder in dry ice to form graphitic mesoporous carbon. Compared with the silica template-guided high temperature graphitization method or transition-metal ion catalytic graphitization methods, this method is energy, material, and labor efficient since the combustion procedure only took about 10 min without any sophisticated equipment or toxic and corrosive reagents (HF). The GPC was then characterized by powder X-ray diffraction (XRD), electron microscopy (TEM, SEM), nitrogen sorption analysis, and Raman spectroscopy. The results demonstrated that the GPC has a high specific surface area and remarkable conductivity. Furthermore, the GPC was used as the working electrode for the simultaneous sensitive determination of dopamine (DA) and uric acid (UA) with the detection limit of 0.008 μM (3 S/N) and 0.03 μM, respectively. Besides, the proposed electrode can be used as an electrochemical sensor for DA and UA detection in real sample analysis.

2 Experimental section

2.1 Chemicals

Magnesium powder of 100–200 mesh (Xilong Chemical Reagent Company Limited, Guangdong, China); phosphate buffer solution (PBS) (Shanghai Kangyi Instrument Company Limited, Shanghai, China); DA and UA were purchased from Sinopharm Group Co., Ltd.

2.2 Instruments and characterization

The X-ray diffractometer was operated at 40 kV and 40 mA with nickel-filtered Cu Kα radiation as the incident beam. A Hitachi s-4800 and a Tecnai F20 were used to investigate the structure and morphology of the GPC; N_2 adsorption–desorption isotherms were obtained at 77 K (Quantachrome NOVA 4000e analyzer). The BET surface area was investigated based on isotherm analysis in a pressure range from 0.04 to 0.9. The pore volumes and relative pore size distributions were derived from the adsorption branches of the isotherms according to the Barrett–Joyner–Halenda model.

2.3 Synthesis of GPC

In a typical experiment, as shown in Scheme 1, 1 kg of dry ice was filled in a 5.0 L beaker. A deep straight hole was dug in the center of the dry ice and 8 g of magnesium powder was put in it. Then, the magnesium powder was ignited and immediately covered up by another dry ice slab (Caution: the reaction is vigorous with lots of heat released and one should keep away). After complete combustion (about 10 min), the crude black composite was obtained. In order to remove the formed MgO and remaining Mg in the composites, the black composite was transferred into a beaker containing 500 mL of 3 M HCl, and then sonicated for 3 h at room temperature. After that, MgO and Mg reacted with HCl to form $MgCl_2$, which could easily be removed after being filtered. The filtrates (isolated GPC) were washed several times until their pH was neutral and then dried under high vacuum overnight at 60 °C.

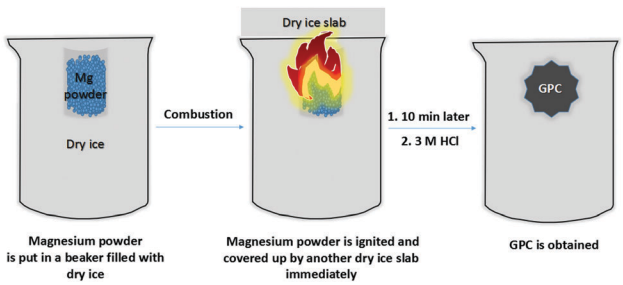

Scheme 1 Synthesis of crude GPC product by the combustion method.

2.4 Electrochemical experiments

Electrochemical experiments were carried out on a CHI 650D electrochemical workstation. Three-electrode system: auxiliary electrode (Pt), working electrode (a bare or modified GCE) and reference electrode (Ag/AgCl). To prepare the working electrode, the GCE was polished to a mirror-like surface with different sizes of γ-alumina slurry (1.0, 0.3 and 0.05 μm), and washed successively with water, ethanol and water in turn. Synthesis of the GPC–chitosan (CS) composite film: 1 mg of GPC and 1 mL of 0.3% CS solution were mixed by ultrasound. Then, 5.0 μL of the above solution was modified on the GCE and dried at 60 °C.

3 Results and discussion

3.1 Characterization

As shown in Fig. 1a, the XRD pattern of the crude carbon/MgO product showed strong and sharp diffraction lines of MgO and graphitic carbon. The results demonstrated the high crystallinity of the carbon/MgO, which might be ascribed to plenty of heat being released during the combustion, facilitating crystallization

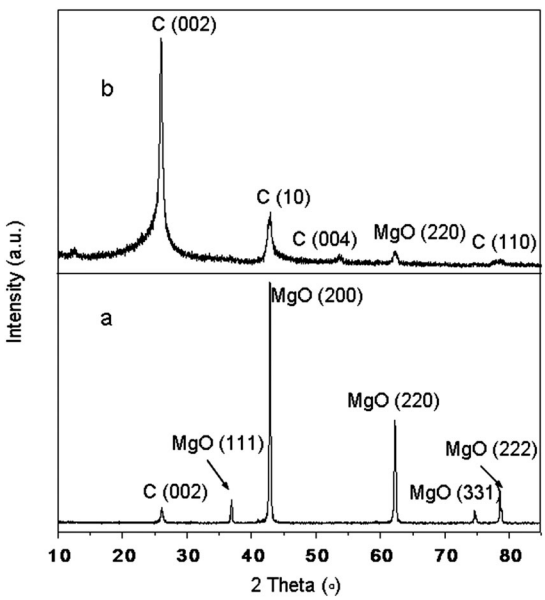

Fig. 1 XRD patterns for the graphitic mesoporous carbon (a) before and (b) after MgO removal.

of the products. After the dissolution of MgO by HCl, GPC was obtained and exhibited XRD peaks at 26.1°, 43.2°, 54.1° and 78.3°, which were attributed to the (002), (10), (004), and (110) diffractions of the graphitic framework of carbon, respectively.[16] Besides, a low MgO diffraction peak at 220 was detected, which was mainly due to the small amount of MgO trapped in the carbon. Moreover, the plane spacing (d_{002}) value was calculated to be 0.35 nm based on Bragg's equation ($n\lambda = 2d\sin\theta$), which was a little larger than the spacing for graphite (0.3354 nm), demonstrating that the graphitic framework of the GPC had turbostratic stacking.[17]

Furthermore, the structure and morphology of the products were investigated by SEM and TEM analysis. Fig. 2a and b show the SEM images of the products before leaching by HCl. The MgO was homogeneously located in the graphitic carbon. After acid leaching, we found the porous graphitic structures with a disordered porosity consisted of a certain amount of macropores (red dashed line in Fig. 2c) and mesopores (Fig. 2d). The mesopore sizes obtained ranged from about 10 nm to 60 nm, which was derived from the MgO template. The macropores might be ascribed to CO_2 gas from dry ice after heating. Furthermore, the fine layered ribbon-like graphitic structures of the GPC could also be seen as shown in the HRTEM images of the GPC in Fig. 2e. The distance between the graphite layers was measured to be 0.35 nm, demonstrating that graphene layer stacking experienced some distortion in the GPC, which was

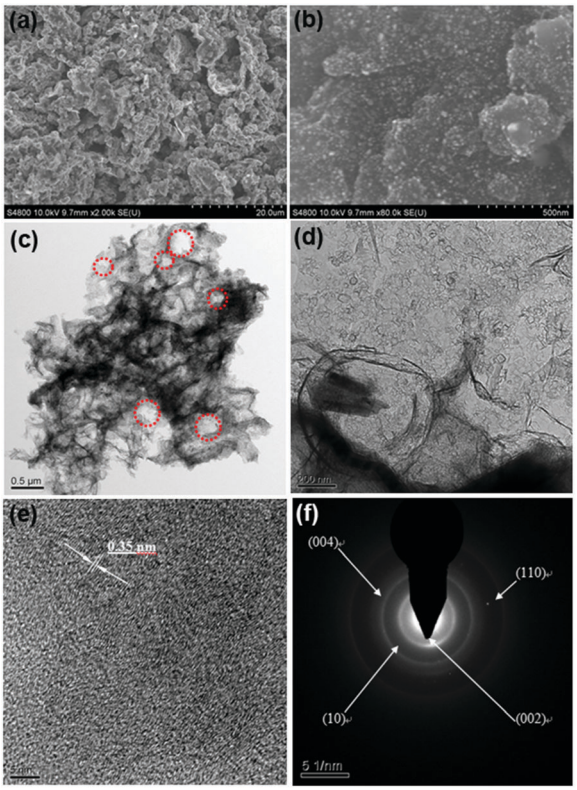

Fig. 2 SEM images of the crude products obtained after combustion consisting of graphitic carbon and MgO before leaching by HCl (a and b); TEM images of the GPC (c and d); HRTEM images of the GPC (e); and SAED pattern of the GPC (f).

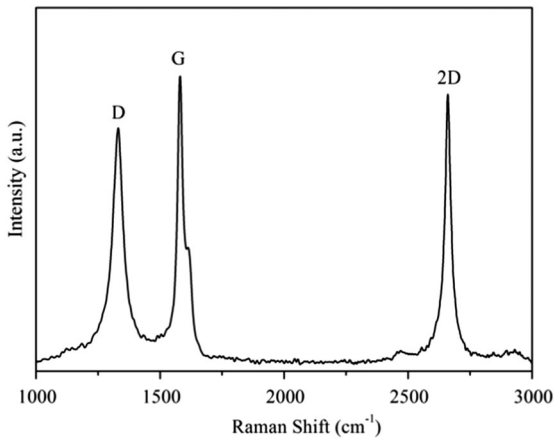

Fig. 3 Raman spectrum of the GPC.

consistent with the $d_{(002)}$ values calculated from the XRD data mentioned above. The SAED pattern of the products revealed a well-defined (002) reflection, with the (10), (004) and (110) rings characteristic of polycrystalline carbon with a high structural organization (Fig. 2f). These results were in good agreement with the above XRD results where the GPC showed high crystallinity. The high graphitic structure of the GPC could be further confirmed by Raman spectroscopy (Fig. 3). The GPC exhibited three distinct peaks at about 1350 cm^{-1}, 1580 cm^{-1}, and 2709 cm^{-1}, corresponding to D-band, G-band and 2D-band, respectively. The relative intensity ratio of I_D/I_G between the D and G bands reflects the degree of graphitization. In this study, the I_D/I_G value of GPC was calculated to be 0.82, suggesting that the GPC had a high degree of graphitization.[18] The results were well consistent with the XRD results and HRTEM analysis mentioned above.

The N_2 adsorption–desorption isotherm analysis of the GPC was carried out and the results are shown in Fig. 4. As shown in the adsorption branch, a clear increase from a relative pressure of 0.9 suggested that the GPC consisted of macropores. These macropores might have resulted from the rapid CO_2 gas emission during magnesium burning with dry ice, which was confirmed

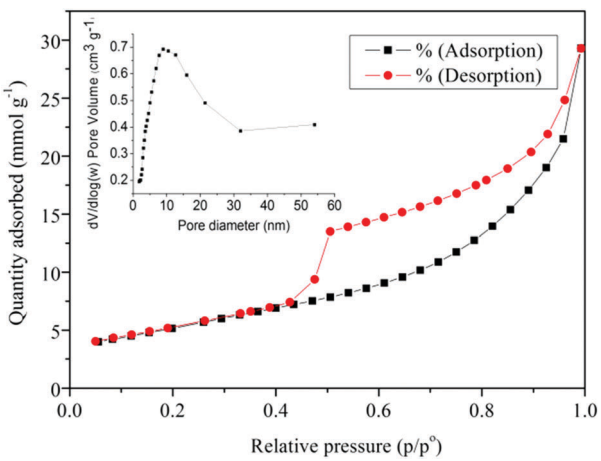

Fig. 4 Nitrogen adsorption/desorption isotherms of the GPC.

Table 1 Comparison of the physical characteristics of the GPC prepared in this study with the other graphitic porous carbons

Sample	S_{BET} (m^2 g^{-1})	V_p (cm^3 g^{-1})	Pore size (nm)	$R = I_D/I_G$	Ref.
GMC[a]	1245	1.47	6.4/1.5	0.94	14
GMC	220	n.d.	8	0.63	19
GPC-2	593	0.74	2, 3.9, 12	1.20	20
GC1000-Fe	49	0.29	n.d.[b]	0.38	21
GC1000-Ni	107	0.52	n.d.	0.66	21
GPC	414.87	1.03	10–60	0.82	This work

[a] GMC: graphitized mesoporous carbon. [b] n.d.: not detected.

by the TEM results in Fig. 2c. At $0.4 < P/P^0 < 0.9$, a hysteresis loop with a pronounced desorption step further demonstrated the presence of mesopores in the GPC. The results were in good agreement with the TEM images in Fig. 2d. Besides, the BET surface area and total pore volume of the GPC were found to be 414.87 m^2 g^{-1} and 1.03 cm^3 g^{-1}, respectively, and the pores were mainly distributed from 10 to 60 nm (inset of Fig. 4) according to the BJH method. The obtained GPC was compared with the other graphitized carbons, and the results are listed in Table 1. The results demonstrated that the obtained GPC had a higher degree of graphitization than GMC-2.3-900 and PGC-2 but with a lower surface area. Conversely, it had a lower degree of graphitization than graphitized mesoporous carbon, GC1000-Fe and GC1000-Ni but with a higher surface area. However, the GPC could be synthesized conveniently in 10 min without any high temperature treatment or catalyst, which was more energy, material, and labor efficient compared with the other methods mentioned in Table 1.[14,19–21]

3.2 Electrochemical properties of GPC–CS/GCE electrode

More and more carbon materials are being applied as highly selective biosensors owing to their simplicity, low cost, fast response, greenness, and high sensitivity.[22–27] Therefore, novel electrochemical biosensors based on GPC may be developed.

As shown in Fig. 5a, the cyclic voltammograms (CVs) were acquired at the bare GCE, CS/GCE and GPC–CS/GCE electrodes in 1.0 mM $[Fe(CN)_6]^{3-/4-}$ solution. On the bare GCE, the oxidative peak current (I_{pa}) and reduction peak current (I_{pc}) were determined to be −2.65 μA and 2.69 μA, respectively. On the CS/GCE, I_{pa} and I_{pc} were decreased to −4.96 μA and 5.31 μA, respectively. The redox peaks increased a little owing to the positively charged CS to negatively charged $[Fe(CN)_6]^{3-/4-}$. On the GPC–CS/GCE, the I_{pa} and I_{pc} are sharply increased to −14.25 μA and 16.23 μA, respectively, which is ascribed to the GPC–CS composite film with high surface area and conductivity accelerating the electron transfer rate. At the same time, the effective surface areas (A) of the GCE, CS/GCE and GPC–CS/GCE electrodes were calculated by the following Randles–Sevcik equation.[22]

$$I_{pa} = 2.69 \times 10^5 n^{3/2} A C_0 D \nu^{1/2}$$

where I_p, D, ν, n, A and C denote the anodic peak current, diffusion coefficient, scanning rate, number of electrons transferred, surface area and concentration of $K_3Fe(CN)_6$, respectively. As is known, $n = 1$ and $D = 7.6$ μcm s^{-1} in a 1.0 mM $K_3Fe(CN)_6$ and 0.1 M KCl mixed solution. Therefore, the microscopic areas can be calculated by $I_{pa} - \nu^{1/2}$ equation (ν is the scan rate). In the bare GCE, $A = 0.041$ cm^2 and for GPC–CS/GCE, A was 0.307 cm^2, which increased nearly 7.0 times. The results explain that the GPC–CS/GCE has an obvious surface area effect and electron-transfer promoting, which can act as a novel electrode for the electrochemical sensors.

Electrochemical impedance spectroscopy (EIS) is further used for the investigation of the electrodes, which can exhibit the impedance changes of the modification processes. Fig. 5b shows the EIS of different electrodes in 1.0 mM $[Fe(CN)_6]^{3-/4-}$ solution. On the GCE, the electrode-transfer resistance value (R_{et}) was 243 Ω while on the CS/GCE the R_{et} value was decreased to 175 Ω, indicating that the presence of CS on the electrode surface could accumulate more $[Fe(CN)_6]^{3-/4-}$ and accelerate the diffusion of ferricyanide toward the electrode surface.[28] What's more, on the GPC–CS/GCE, the R_{et} value was greatly decreased to 46 Ω, which could be attributed to the presence of highly conductive GPC in the composite film that accelerated the electron transfer rate of $[Fe(CN)_6]^{3-/4-}$. The results also strongly proved that the GPC–CS composite could be a promising electrochemical platform for biosensing.

3.3 Cyclic voltammetric behavior of DA and UA on the GPC–CS/GCE

As is known, the I_{pa} for uric acid (UA) and dopamine (DA) are very close to each other on the bare GCE (Fig. 6a).[29] Besides, in order to estimate whether the MgO impurity in the GPC plays a key role for the determination of DA and UA, the performance

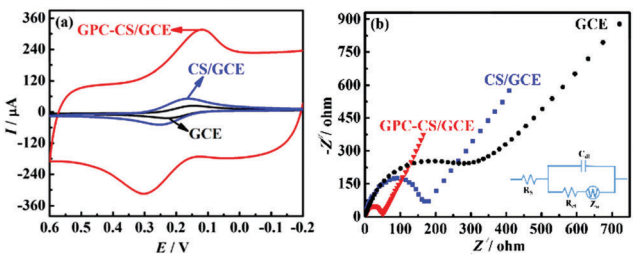

Fig. 5 CV (a) and EIS (b) of 1.0 mM $[Fe(CN)_6]^{3-/4-}$ recorded on bare GCE, CS/GCE and GPC–CS/GCE.

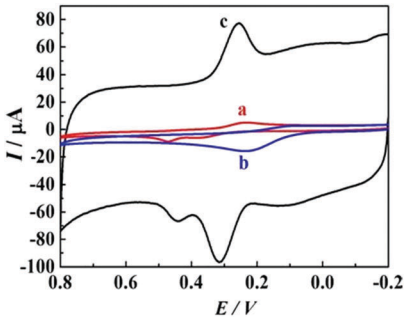

Fig. 6 CV of 0.1 mM DA and 0.1 mM UA recorded on bare GCE (a) MgO-CS/GCE (b) and GPC–CS/GCE (c) in pH 5.0 phosphate buffer solution (scan rate: 0.1 V s^{-1}).

of the MgO nanoparticle-based GCE was also assessed and the results show that the voltammetric peaks of DA, UA overlapped (Fig. 6b). However, on the GPC–CS/GCE they were separated completely into two well-defined peaks with 0.31 V and 0.47 V (Fig. 6c) and the I_{pa} and I_{pc} increased obviously. A possible reaction mechanism of the GPC–CS/GCE with DA and UA was discussed; the π–π stacking interaction between the phenyl of DA and the long range π-conjugation of GPC, which could more easily electrocatalyze the oxidation of DA than that of UA. This is why the oxidation peaks of dopamine and uric acid can be distinguished. Also, it can be concluded that the GPC plays key roles for the determination of UA and DA, rather than the MgO impurity in the GPC. Therefore, the good performance of the GPC–CS/GCE may be attributed to the large surface area, unique structure with mesopores/macropores and turbostratic stacking of the GPC.

3.4 Effect of scan rates and pH

The effect of scan rates (ν) are shown in Fig. 7a. The I_{pa} and I_{pc} increased with the increase of ν ranging from 10 to 500 mV s^{-1}. The peak currents and scan rates had good linear relationships (Fig. 7b and c), suggesting that the oxidations of DA and UA on the GPC–CS/GCE are mainly controlled by a surface-controlled process.[30,31]

Fig. 8a shows the effect of the pH ranging from 4.0 to 10.0 on the GPC–CS/GCE for the 0.1 M PBS, 0.2 mM UA and. 0.2 mM DA solution. The best oxidation peak currents were obtained at pH 5.0. Hence, pH 5.0 was chosen for the electrochemical experiments. Because the H^+ strength and charging states of DA and UA vary with pH, the peak potentials will shift to negative values with the increase of the solution pH.[32] At the same time, the linear relationship equation for the E_{pa} of DA (Fig. 8b) and UA (Fig. 8c) with pH were described as $E_{pa} = -0.0571$ pH + 0.627 ($R^2 = 0.997$) and $E_{pa} = -0.0595$ pH + 0.774 ($R^2 = 0.996$), respectively. The slopes of DA and UA were −57.1 mV per pH and −59.5 mV per pH, respectively, which are close to a Nernst system (−59.0 mV per pH) at 25 °C, showing that the oxidation process is an equal number of electrons.[31–33]

3.5 Simultaneous determination of DA and UA

Differential pulse voltammetry (DPV) was used for the simultaneous determination of UA and DA at the GPC–CS/GCE electrode (Fig. 9), since the DPV method is more sensitive and gives a higher resolution compared to CV. As shown in Fig. 10a, the DPV responses of the GPC–CS/GCE with the different concentration of DA (0.1–250 μM) were recorded in 0.1 M PBS (pH 5.0) and 50 μM UA. A linear plot was obtained between the various concentrations of DA and I_{pa} is $I_{p,DA}$ (μA) = $-5.423 - 0.182C_{DA}$ (μM) ($R^2 = 0.994$) with a detection limit (LD, S/N = 3) of 8.0 nM. Analogously, the DPV responses of the GPC–CS/GCE with different concentration of UA (1.0–400 μM) were recorded in 0.1 M PBS (pH 5.0) and 20 μM DA, and the linear function is $I_{p,UA}$ (μA) = $-0.156 - 0.173C_{UA}$ (μM) ($R^2 = 0.996$) with a LD of 30.0 nM. Comparing with previous works (Table 2),[32,34–44]

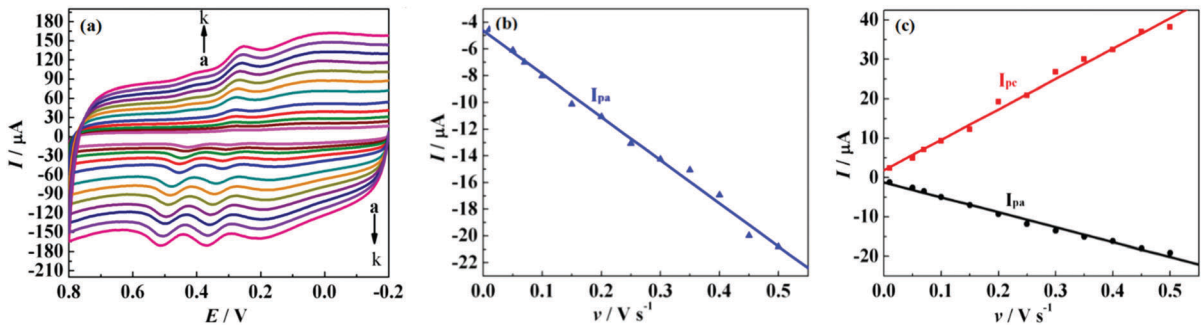

Fig. 7 (a) CV of 0.01 mM DA and 0.1 mM UA on GPC–CS/GCE in pH 5.0 phosphate buffer solution at various scan rates (a–k: 0.01, 0.05, 0.07, 0.1, 0.15, 0.2, 0.25, 0.3, 0.35, 0.4, and 0.45 V s^{-1}). (b) The relationships of UA's I_{pa} with v. (c) The relationships of DA's I_{pa} and I_{pc} with v.

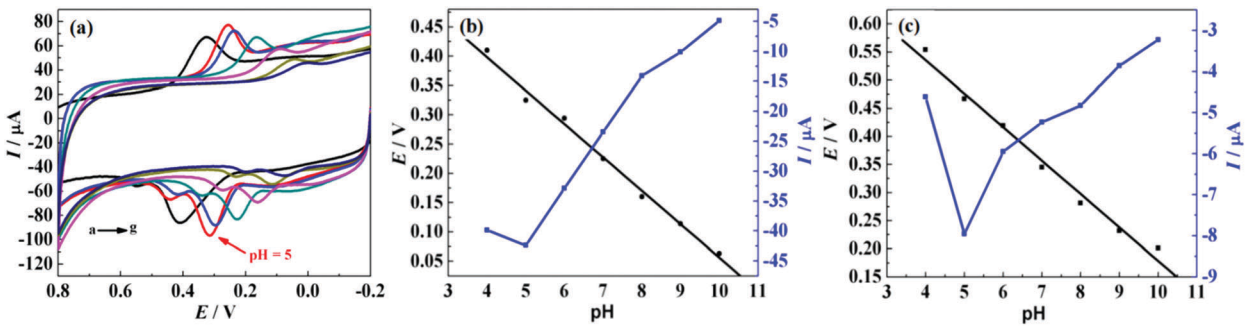

Fig. 8 CV of 0.1 mM DA and 0.1 mM UA recorded on GPC–CS/GCE in pH 4.0–10.0 phosphate buffer solution (a). The relationship of the E_{pa} and I_{pa} against pH (scan rate: 0.1 V s^{-1}) for DA (b) and UA (c).

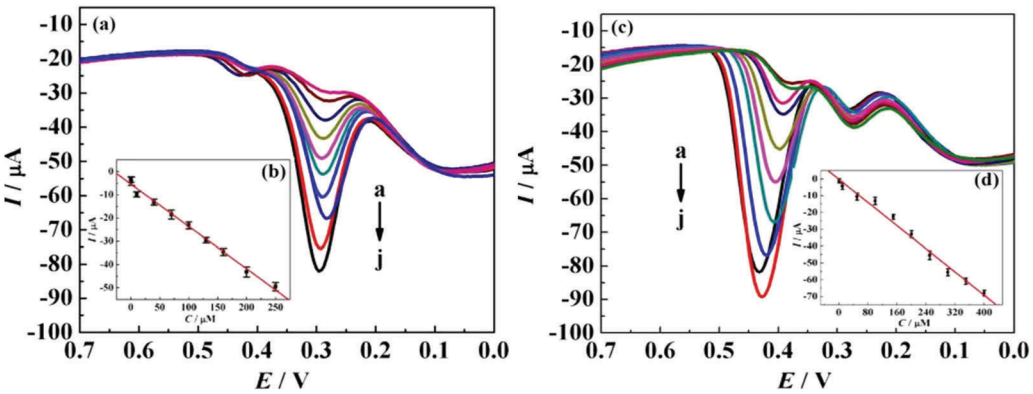

Fig. 9 DPVs at the GPC–CS/GCE electrode in 0.1 M PBS: (a) containing 50 μM UA and different concentrations of DA (from a to j): 0.1, 1, 10, 40, 70, 100, 130, 160, 200, and 250 μM; and (c) containing 20 μM DA and different concentrations of UA (from a to j): 1.0, 10, 50, 100, 150, 200, 250, 300, 350, and 400 μM. Insets: Plots of I_{pa} *vs.* concentration for DA (b) and UA (d).

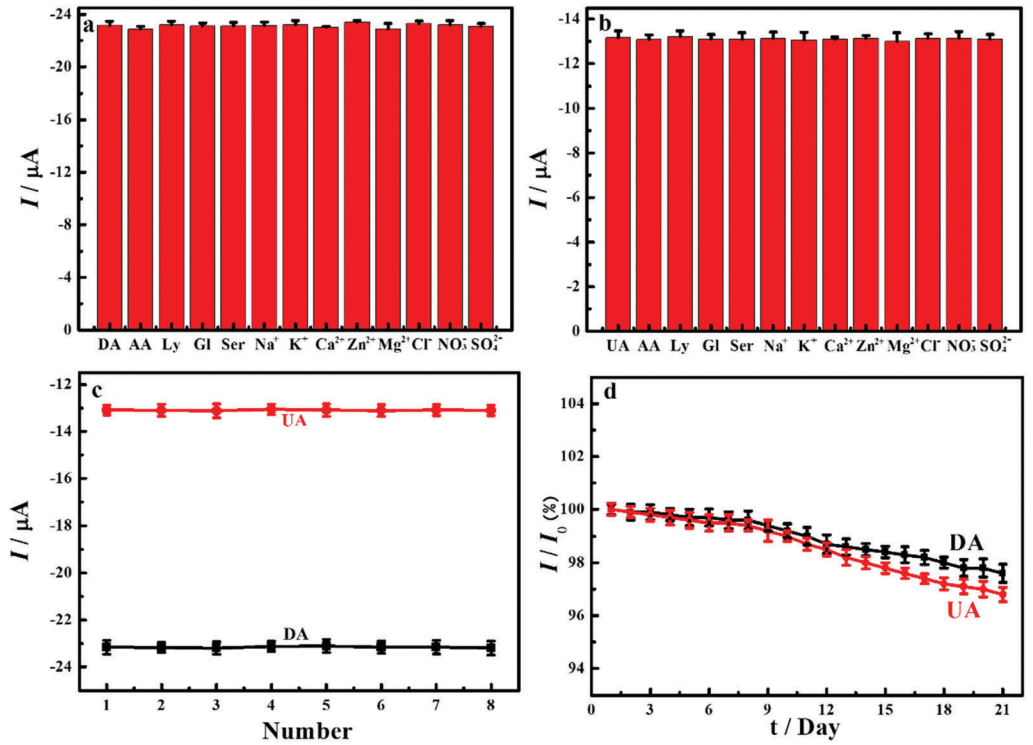

Fig. 10 I_{pa} of 100 μM DA (a) and 100 μM UA (b) in the presence of other biological molecules and ions. (c) The reusability of the biosensors in 100 μM DA, 100 μM UA and 0.1 M PBS. (d) Stability of the biosensors stored at ambient conditions for three weeks.

the simultaneous determination of UA and DA can be achieved using the GPC–CS/GCE electrode.

3.6 Selectivity, reusability and stability of the biosensors

The selectivity, reusability and stability of the biosensors were measured by DPV in this work. As is known, selectivity is an important parameter for biosensors. Therefore, other biological molecules and ions, including ascorbic acid (AA), lysine (Ly), cysteine (Cy), glucose (Gl), serotonin (Ser), Na^+, K^+, Ca^{2+}, Zn^{2+}, Mg^{2+}, Cl^-, NO_3^-, and SO_4^{2-} were investigated in the system. As shown in Fig. 10a and b, the I_{pa} hardly changed in the presence of any of the tested interferents, even at higher concentrations (10 mM) compared to the samples (100 μM DA and 100 μM UA in the pH 5.0 phosphate buffer solution). The results indicated that this system exhibits good selectivity for DA and UA detection.

Fig. 10c shows the DPV response to 100 μM DA and 100 μM UA in pH 5.0 phosphate buffer solution by using eight different GPC–CS/GCE electrodes under the same optimal conditions. The relative standard deviations (RSDs) of DA and UA were 1.26% and 1.87%, respectively. The result demonstrated that the biosensors had very good reusability.

In addition, the GPC–CS/GCE electrode was put into a vacuum drying oven at 25 °C, and the samples (100 μM DA

Table 2 Comparison of the analytical performances of different modified electrodes

	Linear range (μM)		Detection limit (nM)		
Electrode material	DA	UA	DA	UA	Ref.
Flake hexagonal boron nitride	0.5–150	1.0–300	20	150	32
De-bundled single-walled carbon nanotube	5.0–50	5.0–60	15	113	34
3D graphene hydrogel–gold nanoparticles	0.2–30	1.0–60	2.6	5	35
Hierarchical nanoporous PtTi alloy	4.0–500	100–1000	3200	5300	36
Poly(3,4-ethylenedioxythiophene)-graphene	1.0–150	—	330	—	37
Pyrolytic carbon	0.05–1	—	20	—	38
Nitrogen doped porous carbon nanopolyhedra	0.5–30	4.0–50	11	21	39
Nitrogen-doped hierarchically porous carbon	0.05–14.5	2.0–30.0	20	140	40
Porous carbon	0.05–25.0	0.05–30.0	15	10	41
Kiwi skin-derived microporous carbon	2.0–2000	1.0–2500	160	110	42
Nitrogen-co-doped carbon particles	2.0–69.5	5.0–192	340	980	43
Iron–nitrogen co-doped porous carbon	0.5–280	0.5–320	10.6	76.8	44
GPC–CS/GCE	0.1–250	1.0–400	8.0	30	This work

Table 3 Results of determination of DA and UA in DA injection

Sample (μM)	Analyte	Found (μM)	Spiked (μM)	Total found (μM)	Recovery (%)
5	DA	4.98	20	25.42	101.0
	UA	ND	20	19.98	99.9
10	DA	10.01	20	31.05	103.5
	UA	ND	20	19.96	99.8
15	DA	15.02	20	34.99	99.9
	UA	ND	20	20.12	100.6
20	DA	19.97	20	41.03	102.7
	UA	ND	20	19.88	99.4

and 100 μM UA in the pH 5.0 phosphate buffer solution) were determined every day. Fig. 10d shows that the electrode had wonderful stability after 3 weeks: the response of the biosensors to DA and UA had dropped to about 97.6% and 96.8%, respectively. All of the above results show that the biosensors had good selectivity, reusability and stability.

3.7 Real sample analysis

The practical application of the DA and UA sensors was inspected in pharmaceutical preparations. After samples were prepared in accordance with the previous methods,[45] the method was applied to the determination of DA and UA in a DA injection solution. The results are listed in Table 3. The recoveries ranged from 99.4 to 102.7%, which indicated that the GPC–CS/GCE could be successfully used for the determination of DA and UA in DA injection solution.

4 Conclusion

We have demonstrated a simple combustion method for the fabrication of highly graphitic porous carbon with high surface area by using dry ice as a carbon source and magnesium powder as the reductant. The whole combustion procedure only takes about 10 min without any sophisticated equipment or toxic and corrosive reagents, exhibiting high energy, material, and labor efficiency. The GPC obtained consists of highly graphitic nanostructures that exhibit high crystallinity, as shown by TEM, SAED, HRTEM, XRD and Raman analyses. Benefitting from its high crystallinity, the GPC shows high conductivity and could be used as a working electrode for simultaneous, sensitive and selective determination of DA and UA with detection limits (S/N = 3) of 0.008 μM and 0.03 μM, respectively, which are superior to those measured for other carbon nanoparticle-based working electrodes, such as carbon nanotubes and graphenes. The electrode was applied for the determination of UA and DA in real samples.

Conflicts of interest

There are no conflicts to declare.

Acknowledgements

This project was supported by the Education Bureau of Fujian Province (Project No. JAT160302, JAT160875 and JAT171091), the Natural Science Foundation of Zhangzhou (Project No. ZZ2016J31, ZZ2017J20 and ZZ2018J46) and the Training Program Foundation for Excellent Youth Researching Talents of Fujian's Universities (Fujian Education Section, No. 2016-23). This work was also supported by open fund of Fujian Provincial Key Laboratory of Modern Analytical Science and Separation Technology (Minnan Normal University, No. ST201701).

References

1 G. Li, J. Sun, W. Hou, S. Jiang, Y. Huang and J. Geng, *Nat. Commun.*, 2016, **7**, 10601.
2 M. Li, S. Yu, Z. Chen, Z. Wang, F. Lv, B. Nan, Y. Zhu, Y. Shi, W. Wang, S. Wu, H. Liu, Y. Tang and Z. Lu, *Inorg. Chem. Front.*, 2017, **4**, 289–295.
3 Z. Liu, K. Xiao, H. Guo, X. Ning, A. Hu, Q. Tang, B. Fan, Y. Zhu and X. Chen, *Carbon*, 2017, **117**, 163–173.
4 C. Xue, F. Yang, E. Wang, L. Feng, X. Du, X. Hao and X. Li, *Electrochim. Acta*, 2018, **271**, 406–416.
5 F. Ma, D. Ma, G. Wu, W. Geng, J. Shao, S. Song, J. Wan and J. Qiu, *Chem. Commun.*, 2016, **52**, 6673–6676.
6 C. Zhang, R. Kong, X. Wang, Y. Xu, F. Wang, W. Ren, Y. Wang, F. Su and J. X. Jiang, *Carbon*, 2017, **114**, 608–618.

7 X. He, H. Sun, M. Zhu, M. Yaseen, D. Liao, X. Cui, H. Guan, Z. Tong and Z. Zhao, *Chem. Commun.*, 2017, **53**, 3442–3445.
8 M. A. Patel, F. Luo, K. Savaram, P. Kucheryavy, Q. Xie, C. Flach, R. Mendelsohn, E. Garfunkel, J. V. Lockard and H. He, *Carbon*, 2017, **114**, 383–392.
9 S. Li, C. Cheng, H. W. Liang, X. Feng and A. Thomas, *Adv. Mater.*, 2017, **29**, 1700707.
10 X. Xu, Y. Dai, J. Yu, L. Hao, Y. Duan, Y. Sun, Y. Zhang, Y. Lin and J. Zou, *ACS Appl. Mater. Interfaces*, 2017, **9**, 10777–10787.
11 J. N. Wang, L. Zhang, J. J. Niu, F. Yu, Z. M. Sheng, Y. Z. Zhao, H. Chang and C. Pak, *Chem. Mater.*, 2007, **19**, 453–459.
12 Y. Lv, Z. Wu, X. Qian, Y. Fang, D. Feng, Y. Xia, B. Tu and D. Zhao, *ChemSusChem*, 2013, **6**, 1938–1944.
13 S. B. Yoon, G. S. Chai, S. K. Kang, J. S. Yu, K. P. Gierszal and M. Jaroniec, *J. Am. Chem. Soc.*, 2015, **127**, 4188–4189.
14 W. Gao, Y. Wan, Y. Q. Dou and D. Y. Zhao, *Adv. Energy Mater.*, 2011, **1**, 115–123.
15 Y. Liu, Q. Liu, J. Gu, D. Kang, F. Zhou, W. Zhang, Y. Wu and D. Zhang, *Carbon*, 2013, **64**, 132–140.
16 M. Sevilla, C. S. M. Lecea, T. Valdés-Solís, E. Morallónc and A. B. Fuertes, *Phys. Chem. Chem. Phys.*, 2008, **10**, 1433–1442.
17 R. Fu, T. F. Baumann, S. Cronin, G. Dresselhaus, M. S. Dresselhaus and J. J. H. Satcher, *Langmuir*, 2005, **21**, 2647–2651.
18 A. C. Ferrari and J. Robertson, *Phys. Rev. B: Condens. Matter Mater. Phys.*, 2001, **63**, 121405.
19 Y. Y. Shao, S. Zhang, R. Kou, X. Q. Wang, C. M. Wang, S. Dai, V. Viswanathan, J. Liu, Y. Wang and Y. H. Lin, *J. Power Sources*, 2010, **195**, 1805–1811.
20 Z. L. Wang, X. B. Zhang, X. J. Liu, M. F. Lv, K. Y. Yang and J. Meng, *Carbon*, 2011, **49**, 161–169.
21 M. Sevilla, C. Sanchis, T. Valdés-Solís, E. Morallón and A. B. Fuertes, *J. Phys. Chem. C*, 2007, **111**, 9749–9756.
22 X. Yu, W. Zhang, P. Zhang and Z. Su, *Biosens. Bioelectron.*, 2017, **89**, 72–84.
23 Y. Li, P. Zhang, Z. Ouyang, M. Zhang, Z. Lin, J. Li, Z. Su and G. Wei, *Adv. Funct. Mater.*, 2016, **26**, 2122–2134.
24 X. Zhao, P. Zhang, Y. Chen, Z. Su and G. Wei, *Nanoscale*, 2015, **7**, 5080–5093.
25 D. Lin, Z. Su and G. Wei, *Mater. Today Chem.*, 2018, **7**, 76–83.
26 M. Zhang, G. Li, Q. Zhou, D. Pan, M. Zhu, R. Xiao, Y. Zhang, G. Wu, Y. Wan and Y. Shen, *ACS Sens.*, 2018, **3**, 684–691.
27 B. Rezaei and S. Damiri, *Sens. Actuators, B*, 2008, **134**, 324–331.
28 Q. Huang, S. Hu, H. Zhang, J. Chen, Y. He, F. Li, W. Weng, J. Ni, X. Bao and Y. Lin, *Analyst*, 2013, **138**, 5417–5423.
29 L. Wang, X. Qin, S. Liu, Y. Luo, A. M. Asiri, A. O. Al-Youbi and X. Sun, *ChemPlusChem*, 2012, **77**, 19–22.
30 Q. Huang, X. Lin, J. J. Zhu and Q. X. Tong, *Biosens. Bioelectron.*, 2017, **94**, 507–512.
31 S. Hu, Q. Huang, Y. Lin, C. Wei, H. Zhang, W. Zhang, Z. Guo, X. Bao, J. Shi and A. Hao, *Electrochim. Acta*, 2014, **130**, 805–809.
32 Q. Li, C. Huo, K. Yi, L. Zhou, L. Su and X. Hou, *Sens. Actuators, B*, 2018, **260**, 346–356.
33 Q. Guo, T. Wu, L. Liu, H. Hou, S. Chen and L. Wang, *J. Mater. Chem. B*, 2018, **6**, 4610–4617.
34 G. Xu, Z. A. Jarjes, V. Desprez, P. A. Kilmartin and J. Travas-Sejdic, *Biosens. Bioelectron.*, 2018, **107**, 184–191.
35 D. Thirumalai, D. Subramani, J. H. Yoon, J. Lee, H. Paik and S. C. Chang, *New J. Chem.*, 2018, **42**, 2432–2438.
36 Q. Zhu, J. Bao, D. Huo, M. Yang, C. Hou, J. Guo, M. Chen, H. Fa, X. Luo and Y. Ma, *Sens. Actuators, B*, 2017, **238**, 1316–1323.
37 J. Liu, Z. He, J. Xue and T. T. Y. Tan, *J. Mater. Chem. B*, 2014, **2**, 2478–2482.
38 E. Peltola, J. J. Heikkinen, K. Sovanto, S. Sainio, A. Aarva, S. Franssila, V. Jokinen and T. Laurila, *J. Mater. Chem. B*, 2017, **5**, 9033–9044.
39 P. Gai, H. Zhang, Y. Zhang, W. Liu, G. Zhu, X. Zhang and J. Chen, *J. Mater. Chem. B*, 2013, **1**, 2742–2749.
40 A. Nsabimana, J. Lai, S. Li, P. Hui, Z. Liu and G. Xu, *Analyst*, 2017, **142**, 478–484.
41 Q. Cheng, L. Ji, K. Wu and W. Zhang, *Sci. Rep.*, 2016, **6**, 22309.
42 W. Zhang, L. Liu, Y. Li, D. Wang, H. Ma, H. Ren, Y. Shi, Y. Han and B. C. Ye, *Biosens. Bioelectron.*, 2018, **121**, 96–103.
43 H. Guo, M. Wang, L. Zhao, N. Youliwasi and C. Liu, *Microporous Mesoporous Mater.*, 2018, **263**, 21–27.
44 H. Zhou, J. Chen, T. Huang, D. Chen, Y. Wu, F. Zheng, H. Yu and S. Li, *New J. Chem.*, 2017, **41**, 2081–2089.
45 Q. Huang, H. Zhang, S. Hu, F. Li, W. Weng, J. Chen, Q. Wang, Y. He, W. Zhang and X. Bao, *Biosens. Bioelectron.*, 2014, **52**, 277–280.